Lab on a Chip

PAPER

View Article Online
View Journal | View Issue

Cite this: *Lab Chip*, 2024, **24**, 4138

Label-free optical detection of calcium ion influx in cell-derived nanovesicles using a conical Au/PDMS biosensor†

Jisung Kwak,‡[ab] Woochul Kim,‡[a] Hyerim Cho,‡[ac] Jiyun Han,[d] Sang Jun Sim,[b] Hyun Gyu Song,*[a] Yusin Pak*[a] and Hyun Seok Song*[a]

Ion channels, which are key to physiological regulation and drug discovery, control ion flux across membranes, and their dysregulation leads to various diseases. Ca^{2+} monitoring is crucial for cellular signaling when performing Ca-based assays in ion channel research; these assays are widely utilized in both academic and pharmaceutical contexts for drug screening and pharmacological profiling. However, existing detection methods are limited by slow detection speeds, low throughput, complex processes, and low analyte viability. In this study, we developed a label-free optical biosensing method using a conical Au/polydimethylsiloxane platform tailored to detect Ca^{2+} influx in A549-originated nanovesicles facilitated by the transient receptor potential ankyrin 1 (TRPA1) channel. Nanovesicles expressing cellular signaling components mimic TRPA1 signal transduction in cell membranes and improve analyte viability. The conical Au/polydimethylsiloxane sensor converted Ca^{2+} influx events induced by specific agonist exposure into noticeable changes in relative transmittance under visible light. The optical transmittance change accompanying Ca^{2+} influx resulted in an enhanced sensing response, high accuracy and reliability, and rapid detection (~5 s) without immobilization or ligand treatments. In the underlying sensing mechanism, morphological variations in nanovesicles, which depend on Ca^{2+} influx, induce a considerable light scattering change at an interface between the nanovesicle and Au, revealed by optical simulation. This study provides a foundation for developing biosensors based on light–matter interactions. These sensors are simple and cost-effective with superior performance and diverse functionality.

Received 14th May 2024,
Accepted 18th July 2024

DOI: 10.1039/d4lc00421c

rsc.li/loc

Introduction

Ion channels are transmembrane proteins that regulate ion passage across cell membranes and function as crucial drug targets.[1,2] These channels dynamically adjust their open or closed states in response to biological signals such as ligand interactions or membrane potential changes.[3] Proper ion channel activity is fundamental for maintaining physiological processes and cellular homeostasis. Dysregulation of ion channels contributes to disease by causing aberrant ion flux and cellular dysfunction.[4,5]

Ca^{2+} serves as a universal signal transducer or secondary messenger and plays a vital role in regulating various physiological activities. The physiological activities regulated by Ca^{2+} include muscle contraction, neurotransmission, hormone secretion, cell growth and division, and apoptosis. Ca^{2+} binds to troponin in skeletal and cardiac muscles, facilitating muscle contraction.[6] In neurotransmission, Ca^{2+} triggers the release of neurotransmitters at synaptic junctions.[7] It also regulates hormone secretion, such as insulin release in pancreatic beta cells.[8] Additionally, Ca^{2+} signaling pathways control various stages of the cell cycle and cell proliferation.[9] These activities underscore the critical roles of Ca^{2+} in maintaining physiological functions. Changes in intracellular Ca^{2+} concentrations are pivotal for intracellular signaling mechanisms.[10–12] Monitoring these Ca^{2+} levels is essential for understanding cellular mechanisms and responses. Cellular model-based assays for tracking intracellular Ca^{2+} levels are considered as key indicators of ion channel activity in drug discovery research.[1]

Measurement of cellular Ca^{2+} levels and dynamic transitions involves two main methods: fluorescence Ca^{2+} influx assays and patch-clamp recordings. In fluorescence assays, Ca-

---

[a] *Sensor System Research Center, Korea Institute of Science and Technology (KIST), Seoul 02792, Republic of Korea*
[b] *Department of Chemical and Biological Engineering, Korea University, Seoul, 02841, Republic of Korea*
[c] *KU-KIST Graduate School of Converging Science and Technology, Korea University, Seoul, 02841, Republic of Korea*
[d] *Center of Water Cycle Research, Korea Institute of Science and Technology (KIST), Seoul, 02792, Republic of Korea*

† Electronic supplementary information (ESI) available. See DOI: **https://doi.org/10.1039/d4lc00421c**

‡ These authors contributed equally to this work.

sensitive dyes, such as Fluo-4 AM, enter cells and bind to intracellular Ca^{2+}. When triggered by specific agonists or ion channel activators, an increase in Ca^{2+} leads to enhanced fluorescence intensity, which is recorded in real-time using a fluorescence microscope or plate reader.[13] The fluorescent probe has been widely investigated and provides visual and real-time information about Ca^{2+} influx dynamics in various cell type with high temporal resolution.[14] However, the labeling process is essential to detect calcium entering cells, and distribution of the probe is not confined solely to the cytoplasm but also localizes within intracellular compartments such as the endoplasmic reticulum (ER). Given that calcium concentrations are inherently higher in the ER, this results in an elevated background fluorescence signal from these areas, complicating the accurate interpretation of cytoplasmic calcium concentration changes.[15] Furthermore, photo bleaching effect in fluorescent dye restrict the reproducibility and reliability of sensor performance.

Genetically encoded calcium indicators (GECIs) are also innovative tools designed for detailed observation of calcium dynamics within various cell organelles, offering crucial insights into cellular signaling processes. These indicators utilize fluorescent proteins to track calcium changes, enabling precise spatial and temporal analysis of calcium's role in cell physiology.[16,17] Despite their significant contributions, GECIs face challenges such as specific organelle targeting, response kinetics, and potential interference from the organelle's unique environment, which can complicate data interpretation. Especially in cell-based measurement analyses, it is challenging to maintain the viability of cells within various measurement environments. Therefore, it is required to prompt the development of useful biosensor to address the limitation of nanoscale detection and viability of analysis target.

Another common measurement method, patch-clamp recordings offer a direct and precise electrochemical approach for measuring ionic currents induced by changes in Ca^{2+} concentrations. In this method, a high-resistance seal with a single cell membrane is established using a glass (or patch) pipette, and electrical activity in the cell is controlled and recorded by applying a voltage or current clamp.[18] Patch clamps, which based on direct electrode contact, are highly sensitive to cellular ion flux regardless of cellular morphologies, particularly effective in measuring membrane potential occurring at the cell surface. However, at the nano-scale analysis, clamps-based measurement is very limited to precise contact to object surface and high throughput data acquisition.[19,20]

Nanovesicles have emerged as a promising tool for studying ion channels due to their ability to mimic cellular environments while providing stability and control over experimental conditions. Recent advances include nanovesicle-based platforms for ion channel studies. For example, fluorometric functional assays investigate ion channel proteins in lipid nanovesicle membranes, enabling single-molecule analysis of ion flux dynamics.[21] Additionally, single-molecule imaging techniques reveal binding dynamics at cyclic nucleotide-gated ion channels using cell-derived nanovesicles.[22] These platforms allow high-resolution studies of specific ion channel activities and signaling components.

Recent advances in label-free optical biosensing techniques, including surface plasmon resonance (SPR),[23] localized SPR,[24] surface-enhanced Raman scattering (SERS),[25] and ellipsometry-based biosensors,[26] have attracted attention because of their simplicity, rapid response, stability, and cost-effectiveness. Optical methods, which leverage molecular or biophysical properties such as the refractive index and distinctive optical resonance, reduce experimental uncertainties arising from the effect of bound labels on molecular conformation, steric hindrance, and inaccessibility.[27] These sensors respond to specific ligands binding on the biosensing membrane to provide direct information on molecular activities and events in real time.[28] Label-free optical sensors are designed to detect binding interactions between ligands and analytes (protein–protein, enzyme–substrate or inhibitor, protein–DNA, receptor–drug, *etc.*). However, the resolution of sub-molecular events detected using these sensors is still limited because of the size restrictions on analytes, and an additional process is required to immobilize analytes on the biosensing membrane.[29]

In this study, we developed a label-free optical biosensing technique using an Au-decorated conical polydimethylsiloxane (PDMS) sensor (conical Au/PDMS sensor) capable of detecting Ca^{2+} influx in A549 human lung epithelial cell-derived nanovesicles (NVs), which is mediated by the transient receptor potential ankyrin 1 (TRPA1) channel. This channel is a member of the TRP superfamily of ion channels[30] involved in various intercellular signaling pathways, including Ca^{2+} signaling, protein kinase, and pain sensing pathways.[31–33] To enable label-free optical biosensing, we used a conical Au/PDMS structure as a sensing platform, which allowed the analyte to remain stable in solution. When NVs in solution encounter a specific agonist, the resulting Ca^{2+} influx induces an adhesive interaction change between Au and NVs at the interface. This phenomenon was detected as the change in relative transmittance under visible light, which varied from 0.16% to 8.0% and 0.32% to 3.67% depending on the concentration and species of the injected agonist molecule. Relative transmittance changes measured for the conical Au/PDMS sensor were divided into positive and negative terms, indicating the occurrence or absence of Ca^{2+} influx events, respectively. This improved sensitivity and reliability enable the detection of agonist molecules at concentrations as low as 10 pM in approximately 5 s without any immobilization or ligand treatment of the sensor membrane. Our approach ensures the viability of the bioanalytes and supports high-throughput of the method. This method shows potential for detecting targeted molecules and advancing various scientific fields.

Materials and methods

Production of NVs

Adherent A549 cells were cultured in Roswell Park Memorial Institute 1640 medium supplemented with 5% fetal bovine serum, 100 U mL^{-1} penicillin, and 100 μg mL^{-1} streptomycin in a 5% CO_2 atmosphere at 37 °C. The cells were seeded into six-well plates, suspended in serum-free Roswell Park Memorial Institute 1640 medium containing 20 μg mL^{-1} of cytochalasin B (Sigma-Aldrich, St. Louis, MO, USA), and agitated at 300 rpm for 30 min at 37 °C. Next, the NVs were separated from the cells by centrifugation at 1000 rpm for 10 min, after which the supernatant was centrifuged at 4 °C and 14 000 rpm for 30 min to collect the NVs. The prepared NVs were stored at −80 °C and thawed before use.

Fabrication of conical Au/PDMS sensor platform

For biosensor platform fabrication, PDMS was prepared by first mixing SYLGARD 184 A and B (Dow, Midland, MI, USA) in a 10 : 1 weight ratio. The prepared PDMS was poured into a Petri dish, and a micropipette tip was inserted perpendicularly into the PDMS. The 1000 μL micropipette tip which has a length of 100.5 mm and tip radius of 1.36Φ was used for molding. As shown in section S1,† the tip is placed vertically in PDMS elastomer, with its wide end fixed to a flat glass plate and the narrow end is immersed into the PDMS elastomer, serving as the mold. After curing the PDMS at 70 °C for 24 h in a hot oven, the inserted micropipette tip was separated from the PDMS mold. Au (20 nm) was deposited by thermal evaporation (0.7 Å s^{-1}) onto the conical-shaped PDMS mold.

NV characterization

SEM images of the NVs were obtained using a NOVA NanoSEM 200 system (FEI Company, Hillsboro, OR, USA). Fluorescence images of A549 cells before and after Ca^{2+} influx were obtained using a Fluo-4 direct calcium assay kit (Thermo Fisher Scientific, Waltham, MA, USA) and Biotek Synergy HTX multi-mode reader (Winooski, VT, USA). PCR amplification was performed using Maxime PCR Premix (i-StarTaq; iNtRON Biotechnology, Seongnam, South Korea). Quantitative real-time PCR was performed on a real-time PCR system (Applied Biosystems, Foster City, USA) using SYBR Premix Ex Taq (TaKaRa Bio, Shiga, Japan). Each sample was analyzed in triplicate, and the measured mRNA levels were normalized to GAPDH mRNA levels. The liquid AFM images and *F*–*d* curves of the NVs were obtained using a Park NX10 AFM (Park Systems, Suwon, South Korea) with an Au-coated AFM probe (NSC36/Cr–Au). SPR sensing was performed using an iMSPR-mini instrument equipped with a bare Au chip (icluebio, Seongnam, South Korea). Sample preparation details are provided in note S1.†

Device characterization

Cross-sectional scanning electron microscopy and energy-dispersive X-ray spectroscopy elemental mapping of the conical Au/PDMS sensor were conducted using a Regulus8230 FE-scanning electron microscope (Hitachi, Tokyo, Japan). Optical microscopy images were obtained using a material science microscope BX53M (Olympus, Tokyo, Japan). The optical transmittance of the conical Au/PDMS sensor was measured using a UV-vis spectrometer (Ocean Insight, Orlando, FL, USA) equipped with a deuterium–tungsten halogen UV-vis-NIR light source (DH-2000; Ocean Insight). Repeatability was tested by reusing the conical Au/PDMS sensor platform after washing with 70% ethanol in deionized water.

Numerical modeling

Three-dimensional numerical modeling by solving Maxwell's equations was conducted using a commercial finite-difference time-domain program (Lumerical Solutions; Ansys, Canonsburg, PA, USA). We used constant refractive indices for the NVs (1.46) and PBS solution (1.337). Dispersive refractive indices of the Au film and PDMS were experimentally determined as described by Johnson and Christy[34] and Zhang *et al.*[35] The dimensions of the simulated NVs, *i.e.*, radius of 200 nm and maximum aspect ratio of 4, were referred to as the AFM data. Unpolarized plane wave sources were located at the top half of the wavelength, away from the structure. The monitor observing the transmitted light was placed at the bottom half of the wavelength, away from the structure, to exclude the near-field effect. The far-field radiation pattern was calculated as a function of the plane of incidence at a monochromatic wavelength using a monitor.

Results and discussion

NV-based sensing platforms are promising alternatives to conventional living cell-based methods, offering a more stable and efficient means of receptor-dependent signal transduction. This intrinsic ability to amplify signals through intracellular signaling enhances the sensing of molecules, particularly when tailored to receptor-containing properties. A schematic of NV formation is shown in Fig. 1a. Submicron-scale NVs budded from A549 human lung epithelial cells *via* TRPA1 channels. TRPA1 ion channels are present in various tissues and cell types throughout the body, including in sensory neurons, epithelial cells, and immune cells.[36,37] TRPA1 is a polymodal channel, suggesting that it can be activated by a wide range of chemical stimuli such as the agonists allyl isothiocyanate (AITC) and cinnamaldehyde.

These agonistic molecules react covalently with multiple cysteine residues of TRPA1, thereby inducing a conformational change that opens the channel.[38] Consequently, Ca^{2+} influx from the surrounding phosphate-buffered saline (PBS) solution into the NV occurs through open TRPA1. Spherical NVs derived from A549 cells endogenously express the TRPA1 ion channel on their membrane and carry ion channels, G protein-coupled receptors, and the relevant cellular machinery for cyclic adenosine monophosphate signaling. This composition enables NVs to preserve the signal transduction function of TRPA1 channels in cell membranes.[39] Fig. 1b shows scanning electron microscopy images of NVs originating from A549 cells. Dynamic light scattering measurements confirmed that the A549 NVs had an average diameter of 360 nm (section S2†).

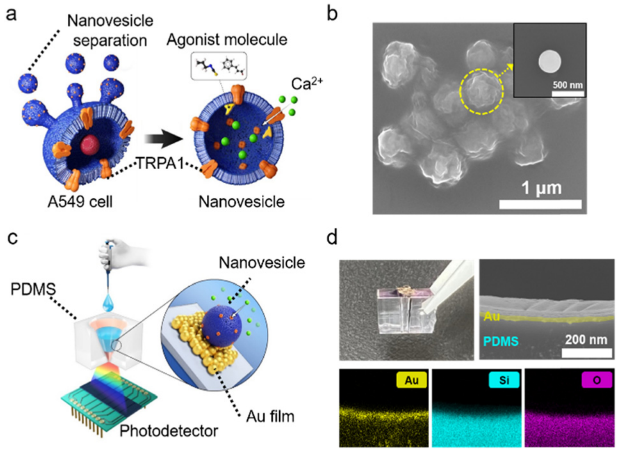

Fig. 1 Configuration of conical Au/PDMS sensor for Ca^{2+} influx detection. a) Schematic of nanovesicle preparation from A549 cell. b) Scanning electron microscopy image of nanovesicles (inset: magnified scanning electron microscopy image of a single nanovesicle). c) Schematic of conical Au/PDMS sensor for detecting Ca^{2+} influx within nanovesicles. d) Images of entire conical Au/PDMS optical sensor (upper left) and cross-sectional scanning electron microscopy image (upper right) and energy-dispersive X-ray spectroscopy elemental analysis (bottom panel) of the Au/PDMS interface.

Fluorescence and patch-clamp methods have advantages and limitations for assessing Ca^{2+} transport. To develop an assay that utilizes the strengths of both techniques, we focused on an approach that demonstrates these advantages using a specific cell type and environmental condition.

To detect Ca^{2+} influx mediated by TRPA1 activation in NVs, we proposed a label-free optical sensing platform based on a conical Au/PDMS sensor, as illustrated in Fig. 1c. NV-suspended PBS solution was first injected into the conical Au/PDMS cavity, followed by introduction of agonist molecules to activate TRPA1. The conical shape of the PDMS cavity and thin Au layer inside were designed to hold the NV-suspended solution *via* an electrostatic adhesive force. In addition, the hydrophobic nature of the PDMS surface contributed to the formation of an adhesive solution without distortion. The solution was positioned near the central region of the PDMS cavity and featured a conical void beneath it. The top of the Au/PDMS sensor was exposed to white light, and a photodiode array positioned below the Au/PDMS sensor assessed the transmitted light intensity, facilitating quantification of Ca^{2+} influx into the NVs. Multiple nanovesicles are attached to the Au film, and the conical Au–PDMS biosensor detects the average optical effect generated by the numerous nanovesicles due to Ca influx. The inset figure of Fig. 1c showed an enlarged schematic of one of the many adsorbed nanovesicles.

Fig. 1d shows an image (top left) of the conical Au/PDMS sensor, which had upper and bottom hole diameters of 2.3 and 1.3 mm, respectively, and a vertical length of 5 mm (section S3†). The cross-sectional scanning electron microscopy images revealed uniform coverage of the inner surface of the conical Au/PDMS sensor with a 20 nm thick Au layer, intended as binding sites for the NVs. The direction of cross-sectional view is shown in section S4.† The elemental distribution was investigated using energy-dispersive X-ray spectroscopy (lower panel of Fig. 1d), which confirmed the uniform distribution of Au (yellow) on the PDMS surface, represented by silicon (sky blue) and oxygen (purple).

Before assessing Ca^{2+} influx using the Au/PDMS sensor, the effect of AITC and cinnamaldehyde agonists on TRPA1 responses in A549 cells and NVs was verified using conventional fluorescence assays, as shown in Fig. 2. Injection of AITC and cinnamaldehyde into each A549 cell sample at concentrations of at least 10^{-2} M markedly increased the fluorescence intensity (Fig. 2a and section S5†). Lower AITC concentrations in the range of 10^{-2}–10^{-5} M elicited a comparatively moderate fluorescence response. This pronounced response signifies the robust electrophilic properties of AITC in activating the TRPA1 channel, thereby facilitating rapid influx of Ca^{2+} into the cell. The A549 cell-derived NVs possessed intracellular signaling components, such as ion channels, on their surface. Fig. 2b shows the temporal decline in fluorescence intensity after injecting agonists into the NVs. The slow and incomplete recovery of the initial fluorescence intensity may be attributed to the inability of the NVs to expel Ca^{2+} because of the absence of ion pumps and calmodulin.

We performed polymerase chain reaction (PCR) to confirm TRPA1 expression within A549 cells. As shown in Fig. 2c and d, we examined TRPA1 mRNA levels across various cell types.

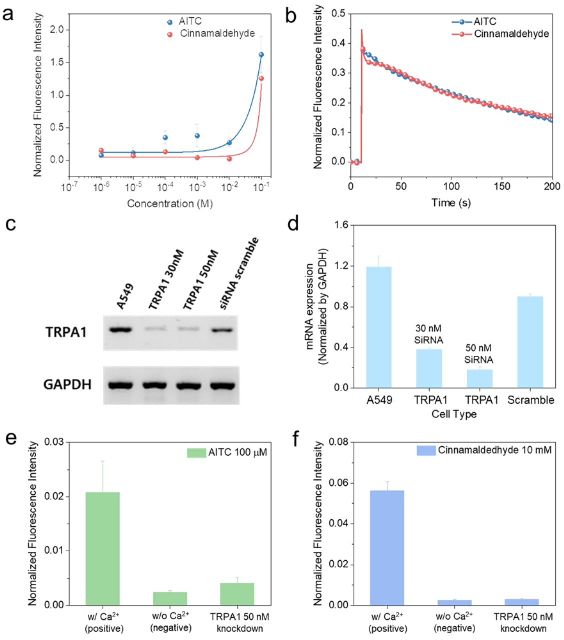

Fig. 2 Characterization of nanovesicle considering Ca^{2+} influx. a) Dose-dependent Ca^{2+} influx into A549 following AITC and cinnamaldehyde treatment. b) Time-dependent Ca^{2+} influx into A549 nanovesicles post-AITC and cinnamaldehyde addition. c) PCR for TRPA1 expression post-siRNA. d) Real-time PCR showing reduced TRPA1 mRNA. Ca^{2+} influx into nanovesicles following e) AITC (100 μM) and f) cinnamaldehyde (10 mM) addition.

Considering the ubiquitous nature of TRPA1 in multiple cell types, we used small interfering RNA (siRNA) aimed at TRPA1.[36,40] Incorporating siRNA targeting TRPA1 was crucial for understanding specific effects and for confirming the accuracy of our findings. We determined the optimal concentration for gene silencing using quantitative real-time PCR. We also assessed the effectiveness of siRNA knockdown by adjusting its concentration and compared the results with those obtained using a control with a scramble sequence.

As shown in Fig. 2e and f, Ca^{2+} influx assays were performed using NVs derived from A549 cells under three distinct conditions:

i) *Positive control*: A549 NVs were resuspended in PBS containing Ca^{2+} (w/Ca^{2+}).

ii) *Negative control*: A549 NVs were resuspended in PBS without Ca^{2+} (w/o Ca^{2+}).

iii) *Knockdown control*: A549 NVs subjected to 50 nM siRNA knockdown were resuspended in PBS containing Ca^{2+} (w/Ca^{2+}).

Upon exposure to 100 μM of the agonist AITC (Fig. 2e), the NVs resuspended in PBS with Ca^{2+} showed the highest normalized fluorescence intensity, reflecting significant Ca^{2+} influx. In contrast, the response was reduced for NVs from siRNA-knockdown cells in PBS with Ca^{2+}. The lowest influx was observed for NVs in PBS without Ca^{2+}. A similar trend was observed for cinnamaldehyde at 10 mM (Fig. 2f), with the NVs in PBS containing Ca^{2+} exhibiting the most pronounced Ca^{2+} influx. This differential Ca^{2+} influx emphasizes the relationship between TRPA1 activity and the presence of extracellular Ca^{2+}. Specifically, the robust response of A549 NVs to PBS with Ca^{2+} demonstrates the role of TRPA1 channels in facilitating Ca^{2+} influx when exogenous Ca^{2+} is present. However, the diminished response in siRNA-knockdown NVs, even in the presence of Ca^{2+}, suggests that 50 nM siRNA treatment affected the function of TRPA1, likely reducing its expression and the number of channels available for Ca^{2+} transport.

To verify the optical sensing properties Ca^{2+} influx, we investigated changes in relative transmittance (ΔT) at wavelengths of 400–500 nm before and after introducing agonist molecules (Fig. 3a and b). Three different samples representing positive, negative, and knockdown were compared to determine the sensing reliability of the Au/PDMS sensor. After introducing 1 μM AITC, the ΔT of the positive control sample increased asymmetrically in the range of 400–500 nm, with a ΔT peak of 1.26% at 447 nm (Fig. 3a). Compared with that in the positive control sample, ΔT decreased by 0.06% and 0.31% at 447 nm in negative and knockdown control samples, respectively, following treatment with AITC. When 1 μM of cinnamaldehyde was introduced, a spectral pattern analogous to that of AITC treatment was observed (Fig. 3b). The positive control sample exhibited an increase in ΔT of up to 1.06% at 447 nm. In contrast, the negative and knockdown controls showed decreases in ΔT of −0.09% and −0.14%, respectively. In the range of 400–500 nm, the Ca^{2+} influx response exhibits a characteristic peak increase centered around 470 nm. This is presumed to result from a specific reaction rather than a broad scattering induced by simple changes in solution volume. As a primary sensing metric to accurately measure Ca^{2+} influx in NVs while minimizing signal noise, we selected ΔT at a wavelength of 447 nm, as it showed the largest deviation.

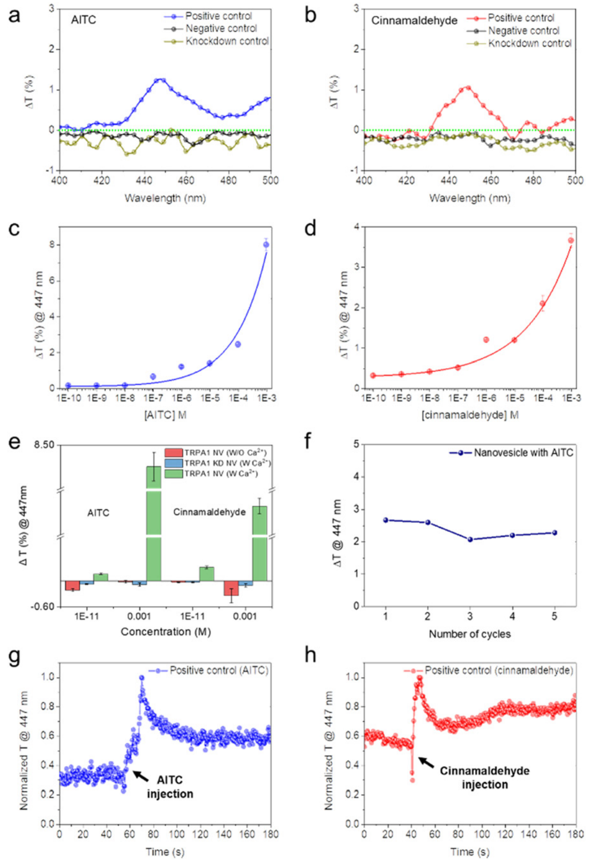

Fig. 3 Sensing properties of conical Au/PDMS sensor. Relative transmittance changes (ΔT) after introducing a) AITC and b) cinnamaldehyde under three different sample conditions: i) positive, ii) negative, and iii) knockdown controls. ΔTs at a wavelength of 447 nm depending on the concentration of c) AITC and d) cinnamaldehyde. e) Comparison of ΔT at 447 nm of TRPA1 NV (w Ca^{2+}), TRPA1 knockdown (KD) NV (w Ca^{2+}), and TRPA1 NV (w/o Ca^{2+}) f) repeatability test for evaluating the sensing capabilities of a conical Au/PDMS biosensor. Normalized transmittance at 447 nm with time after g) AITC and h) cinnamaldehyde treatment.

Fig. 3c and d show the concentration dependence of ΔT at a wavelength of 447 nm on the agonist molecules of five positive control samples at each concentration. As the concentration of AITC was increased from 10 pM to 1 mM, the average ΔT value gradually increased from 0.16% to 8.0% (Fig. 3c). Similarly, the average ΔT with increasing cinnamaldehyde concentrations increased from 0.32% to 3.67% (Fig. 3d). The relationship between ΔT and agonist concentration indicates that the transmittance changes of the conical Au/PDMS sensor are directly related to the amount of Ca^{2+} influx into the NV. By estimating the effective agonists per nanovesicle, the correlation between concentration of agonist and number of nanovesicle which is induced Ca^{2+} influx, can be evaluated (note S2†). In our nanovesicle/agonist system, the effective agonist per nanovesicle in unit volume is 6.6 and 5.8×10^4 for AITC and cinnamaldehyde, respectively. When 100 pM of agonist is introduced, it is estimated that effective Ca influx event occurs in approximately 9.8×10^5 and 1.0×10^4 nanovesicles on the Au–PDMS biosensor for AITC and cinnamaldehyde, respectively.

To further investigate the effects of negative and knockdown control samples, the average ΔT values at 447 nm of five samples were measured under 10 pM [low concentration (low conc.)] and 1 mM [high concentration (high conc.)] agonist treatments. Their average ΔT values were compared to that of positive sample, as shown in Fig. 3e and section S6.† For AITC, the ΔT values decreased to −0.02% (high conc.) and −0.21% (low conc.) in the negative controls and −0.08% (high conc.) and −0.07% (low conc.) in the knockdown samples. On the other hand, the positive controlled sample exhibited 0.16 and 8.0% increase of ΔT in low and high concentration of agonist, respectively. After introducing cinnamaldehyde, ΔT decreased to −0.03% (high conc. in the negative control), −0.03% (low conc. in the negative control), −0.34% (high conc. in the knockdown control), and −0.1% (low conc. in the knockdown control). On the contrary, the ΔT of positive controlled sample increased 0.32 and 3.66% in low and high concentrations, respectively.

The consistent decreases in ΔT for both TRPA1 knockdown and negative control samples result from the light scattering effect due to solution volume expansion following agonist injection, with the former experiencing reduced calcium entry channels due to TRPA1 suppression by specific siRNA, and the latter lacking available calcium despite the presence of TRPA1 channels, ultimately leading to similar light scattering phenomena in both cases.[41,42] The optical scattering effect by volume expansion of solution can be verified in ΔT variation of non-NV contained solution. The ΔT of the PBS solution without NVs also negatively changed after AITC and cinnamaldehyde treatment (section S7†). The conical Au/PDMS biosensor measures the relative transmittance changes before and after Ca^{2+} influx in response to agonist injection. In the positive control, there is always a positive change to detection limit, whereas in other samples, there is consistently a negative change, which is useful for setup a baseline.

To investigate the reusability of conical Au/PDMS biosensor, repeatability tests were conducted by reusing the conical Au/PDMS sensor and washing it with 70% ethanol solution. As shown in Fig. 3f, the ΔT remained relatively constant with a standard error of 0.12% over five cycles, demonstrating the consistent repeatability of the biosensor and providing a cost-saving strategy in biosensing technology. The weak binding between gold and NV facilitates easier cleaning with ethanol, and since no labelling process is performed on the gold surface, the sensor's stability is ensured.

Response time is another important factor in biosensing technologies in terms of high-throughput screening. Fig. 3g and h showed the normalized transmittance changes over time in positive control samples after agonist introduction, which were used to analyze the response time of the conical Au/PDMS sensor. The normalized transmittance at 447 nm instantly increased to its maximum peak point at 14 and 5 s after AITC and cinnamaldehyde injection, respectively. In negative and knockdown control samples, transmittance decreased within 18 and 11.5 s, respectively (Sections S8 and S9†).

To gain more detailed insights into the detection mechanism of the conical Au/PDMS sensor, we investigated the underlying physical interaction between Au and NVs depending on Ca^{2+} influx. First, the physical binding characteristics between bare Au and NVs were analyzed using SPR measurements (Fig. 4a). On bare Au film, the fixation/binding of NV with and without the TRPA1 channel occurred at 2500 and 2200 resonance units, respectively, and the reaction time was approximately 8000 s at 10 μL min^{-1} of continuous PBS solution flow. From ‘a’, NVs began to be injected, and the binding events are represented as peaks in ‘b’ and ‘c’ in the inset. The results indicate that NVs can bind to the Au surface regardless of the presence of TRPA1 channels. The intrinsic adhesion of the NVs for bare Au surface is attributed to electrostatic interaction between bare Au surface and electrically charged lipid membrane and protein on NV surface.[43,44]

Liquid atomic force microscopy (AFM) was performed to measure the adhesive energy between the Au-coated AFM tip

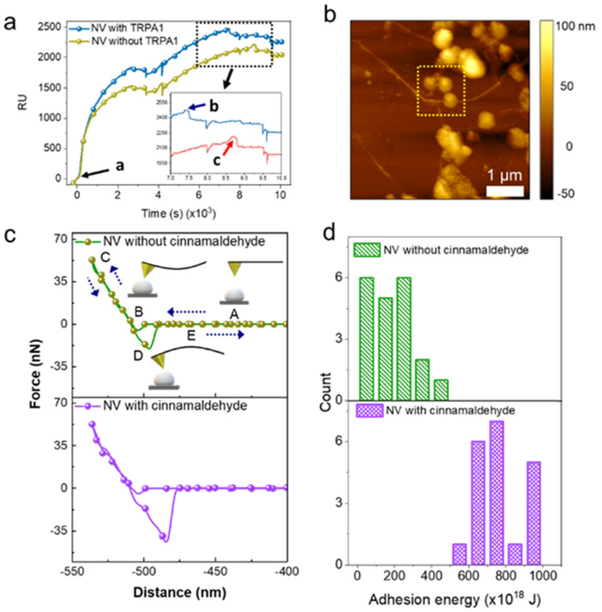

Fig. 4 Adhesive interaction of nanovesicles considering Ca^{2+} influx. a) Surface plasmon resonance analysis of nanovesicles with and without TRPA1 on bare Au film where (a) is injection time of NVs (inset: magnified surface plasmon resonance peaks represented as (b) and (c) in the range of 7–10 s). b) Liquid atomic force microscopy image of nanovesicles immersed in 1 mM $CaCl_2$-dissolved phosphate-buffered solution. c) Force–distance curve of nanovesicles under exposure without (upper panel) and with (lower panel) cinnamaldehyde. (A)–(E) represent each interaction event point as the AFM tip approaches the NV surface. d) Adhesion energy distribution for 20 nanovesicles under exposure without (upper panel) and with (lower panel) cinnamaldehyde.

and single NVs. To consider the effect of Ca^{2+} influx, the NVs were fully immersed in 1 mM $CaCl_2$ dissolved in PBS, and cinnamaldehyde was injected into the solution to induce TRPA1 channel activation. Spherical NVs with a diameter of 400 nm are shown in the liquid AFM image in Fig. 4b (highlighted in the yellow box). The force–distance (*F*–*d*) curve was measured in three sequences: (1) tip approach, (2) direct contact between the tip and the NV surface, and (3) tip retraction. The curve, which records the applied force as a function of tip–surface separation, provides mechanical information on the tip–surface interactions. The *F*–*d* curves of the NVs with and without cinnamaldehyde are shown in Fig. 4c. After the AFM tip approached the NV surface (A), the tip–surface interaction caused the tip to contact the NV surface (B). The tip and sample were in contact and bent upward upon further movement of the z-piezo (C). At the maximum point, the tip did not bend as it moved away from the surface. The tip stuck to the adhesive dip before being released from the interface (D). Finally, the tip returned to its unperturbed state (E). The shape of the *F*–*d* curve is highly dependent on the interaction between the tip and NV surface. For example, a sample with high adhesion requires a higher force to separate the tip from the sample than from a sample with low adhesion, resulting in a larger amplitude in the negative direction. The NVs with non-activated TRPA1 (without cinnamaldehyde) showed small tip separation movement at D (upper panel of Fig. 4c). In comparison, larger tip movement during the withdrawal sequence was observed on NVs with cinnamaldehyde (lower panel of Fig. 4c). The large negative force in the tip-withdrawal state indicates that Ca^{2+} introduced into the NVs strongly affected the adhesive interaction between NVs and bare Au.

The adhesion energy is reflected as the area between the retracted curve and baseline in the *F*–*d* curve. Fig. 4d shows the distribution of the adhesion energy calculated from the *F*–*d* curves of 20 NVs. The adhesion energies of the NVs without cinnamaldehyde (no Ca^{2+} influx) were $12–316 \times 10^{18}$ J, with an average value of 184×10^{18} J. In contrast, the NVs containing Ca^{2+} had a larger average energy of 762×10^{18} J with a range of $559–991 \times 10^{18}$ J. The liquid AFM results demonstrated that NVs experiencing Ca^{2+} influx exhibited approximately 4.14-fold increase in adhesion energy compared to those not occurring Ca^{2+} influx. As local positive charge on the NV surface and surroundings becomes weakened, the space charge which hinder the electrostatic adhesion between NV and Au surface. As consequence, the contact area and adhesion energy between NV and metal surface increase.[44–46] Based on the experimental findings and related literatures, we estimated that the large difference in adhesion energy between Au and NV stems from distinct Ca^{2+} distributions inside and outside NV induced by Ca^{2+} influx. The hypothetical illustration is shown in Fig. 5a.

The schematic in Fig. 5a shows the transition of NV adhesion depending on the Ca^{2+} distribution. Because the NVs were surrounded by Ca^{2+}-containing PBS solution, the interface between the Au and the NV surface was filled with Ca^{2+}. Upon activation of the TRPA1 channel by agonist molecules, Ca^{2+} influx into the NVs induced a local decrease in the ion concentration at the interface, reducing the screening effect exerted by Ca^{2+} and hindering the attraction of Au and the NVs. An increase in the adhesion energy between them increased the effective adhesion area at their interface and influenced the final morphology of the adhered NV.[47] Because of the high adhesion, the shape of the NVs changed from spherical to elliptical as the adhesive area of the NVs on the substrate increased.[48] Notably, this strong correlation between the Ca^{2+} density and NV shape changes made it possible to conduct finite-difference time-domain simulation.

To identify the origin of the increase in the transmitted light, we simplified the geometry of the NV as an ellipse (Fig. 5b). As the ion density increased, the corresponding aspect ratio of the ellipse also increased. The volume of the NVs did not vary with respect to the ion density. Fig. 5c shows the results of the finite-difference time-domain simulation with respect to the aspect ratio. To simplify the complex condition, we assume a single nanovesicle with a radius of 200 nm attached to the Au film on PDMS with an inclined angle of 78 degrees, which is a representative angle owing to the accumulation of PBS solution in the central part of the structure (section S10†). The simulated spectral aspect agreed well with the experimental data. The Au film in the visible range exhibited not only the properties of a lossy dielectric in the blue region, but also metallic properties in the red region. In the dielectric region, the variation in transmittance noticeably increased compared with that in the metallic region, demonstrating independence from the

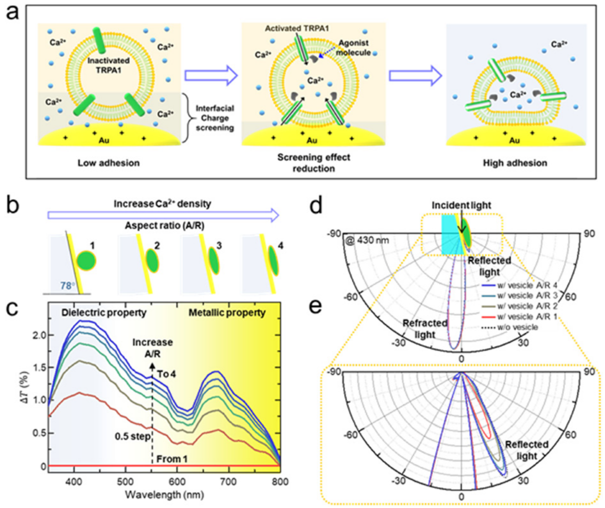

Fig. 5 Simplified modeling of nanovesicles in relation to Ca^{2+} density using finite-difference time-domain simulation. a) Schematic of the morphological variation of nanovesicles on the Au surface depending on the Ca^{2+} distribution. b) Schematics of variation of the aspect ratio of nanovesicles in relation to the Ca^{2+} density. c) Results of finite-difference time-domain simulation for variation of forward scattered light. d) Far-field pattern at 430 nm depending on the aspect ratio (e) inset: massive increase in reflected light as the aspect ratio was increased).

plasmonic effect. To identify the origin, we extracted the far-field radiation patterns at 430 nm, as shown in Fig. 5d. Transmitted light is mainly composed of two components: refracted light passing through a negative angle and reflected light from the interface propagating at a positive angle. As shown in the inset of Fig. 5e, the intensity of the reflected light only increased as the aspect ratio of the NVs increased. The FDTD simulation for diverse angles, 80°, 75°, and 70°, respectively were conducted in section S11.† In a visible range (dielectric property of gold), transmittance increase as aspect ratio increase for all angles owing to reduced scattering effect. On the other hands, in a near IR range (metallic property of gold), transmittance decrease as aspect ratio increase for 70° and 75° owing to surface plasmon resonance effect. Therefore, our interest is only in the visible range so that transmittance always increases depending on aspect ratio for all three angles. Eventually, the intensity at an aspect ratio of 4 converged to that of the Au thin film on PDMS without NVs. Considering a single NV on the Au substrate, the incident light was strongly scattered by the NVs. However, when the NVs became elliptical, the scattering effect was eliminated, and the reflected light was strongly enhanced. Hence, the enhanced reflected light induced an increase in the transmitted light.

Conclusions

We developed a biosensor using a conical Au/PDMS sensing platform to detect Ca^{2+} influx within NVs derived from A549 human lung epithelial cells. We introduced a conical Au/PDMS structure to stably hold the analyte solution. To improve the stability and reliability of the biosensor, NVs with an average diameter of 360 nm were used to provide a stable membrane environment for the TRPA1 ion channel to facilitate Ca^{2+} influx. When the NVs were exposed to specific agonists, including AITC and cinnamaldehyde, the relative optical transmittance of TRPA1-expressing NVs in the conical Au/PDMS platform significantly increased in response to Ca^{2+} influx. In contrast, transmittance decreased in NVs with suppressed TRPA1 or non-Ca^{2+}-containing samples. This feature enabled the screening of Ca^{2+} influx and TRPA1 functionality in NVs with high accuracy. Liquid AFM measurements demonstrated that the adhesion energy of the NV surface increased by approximately 4-fold upon the introduction of Ca^{2+}, and optical simulation analysis was performed based on this phenomenon. The adhesion energy induced a change in the NV shape from sphere to ellipsoid. Morphological variations resulted in significant optical scattering at the Au/NV interface, leading to a corresponding change in transmittance. The conical Au/PDMS sensor exhibited a linear relationship with the change in transmittance depending on agonist molecule concentration. The response time was measured as 14 and 5 s following AITC and cinnamaldehyde treatment, respectively, which is higher than the detection rate of other techniques. These results can advance label-free optical biosensor and its applications, enabling rapid detection, high-throughput screening, and improvement in accuracy, thereby complementing conventional biosensor techniques such as fluorescent probes, GECIs, and patch clamp. The figure-of-merits and limitations of representative Ca^{2+} influx detection methods are summarized in Table S1.† Moreover, the simple preparation process without immobilization or labeling process and the reliable repeatability of our biosensor will promote the development of cost-effective and universal biosensor technologies. Specifically, our biosensor is designed to monitor calcium influx in nanovesicles, which is crucial for screening drugs targeting ion channels. By allowing real-time monitoring of these effects, it can help identify potential drug candidates that modulate ion channel activity.

Data availability

Data underlying the results presented in this paper are not publicly available at this time but may be obtained from the authors upon reasonable request.

Author contributions

J. K., W. K., and H. C. contributed equally to this study. J. K., W. K., and H. C. conceived the study, performed the experiments, and wrote the manuscript. J. H. and S. J. S. contributed to the discussion of biosensing and device characterization. H. G. S. contributed to the computational analysis of the optical simulation and the underlying mechanism. H. G. S, Y. P., and H. S. supervised and coordinated the study. All authors discussed, commented on, and revised the final manuscript. These authors contributed equally.

Conflicts of interest

There are no conflicts to declare.

Acknowledgements

This work was supported by the National Research Foundation of Korea (NRF) grant funded by the Korean Government (MSIT) (No. RS-2023-00302397, 2020M3H5A108110421) and the National Research Council of Science & Technology (NST) (CAP22012-000).

References

1 S. K. Bagal, A. D. Brown, P. J. Cox, K. Omoto, R. M. Owen, D. C. Pryde, B. Sidders, S. E. Skerratt, E. B. Stevens and R. I. Storer, *J. Med. Chem.*, 2013, **56**, 593–624.

2 B. Hille, *Biophys. J.*, 1978, **22**, 283–294.

3 J. J. Clare, *Discov. Med.*, 2010, **9**, 253–260.

4 A. R. Ednie and E. S. Bennett, *Compr. Physiol.*, 2011, **2**, 1269–1301.

5 I. Splawski, K. W. Timothy, L. M. Sharpe, N. Decher, P. Kumar, R. Bloise, C. Napolitano, P. J. Schwartz, R. M. Joseph and K. Condouris, *Cell*, 2004, **119**, 19–31.

6 D. E. Clapham, *Cell*, 2007, **131**, 1047–1058.

7 T. C. Südhof, *Annu. Rev. Neurosci.*, 2004, **27**, 509–547.

8 P. Rorsman and M. Braun, *Annu. Rev. Physiol.*, 2013, **75**, 155–179.

9 M. J. Berridge, P. Lipp and M. D. Bootman, *Nat. Rev. Mol. Cell Biol.*, 2000, **1**, 11–21.

10 R. Barhoumi, Y. Qian, R. C. Burghardt and E. Tiffany-Castiglioni, *Neurotoxicol. Teratol.*, 2010, **32**, 16–24.

11 G. Carmeliet, S. Van Cromphaut, E. Daci, C. Maes and R. Bouillon, *Best Pract. Res., Clin. Endocrinol. Metab.*, 2003, **17**, 529–546.

12 G. C. Terstappen, R. Roncarati, J. Dunlop and R. Peri, *Future Med. Chem.*, 2010, **2**, 715–730.

13 K. R. Gee, K. Brown, W. U. Chen, J. Bishop-Stewart, D. Gray and I. Johnson, *Cell Calcium*, 2000, **27**, 97–106.

14 D. L. Armstrong, C. Erxleben and J. A. White, in *Methods in cell biology*, Elsevier, 2010, vol. 99, pp. 183–197.

15 M. Whitaker, in *Methods in cell biology*, Elsevier, 2010, vol. 99, pp. 153–182.

16 N. Wu, W. K. Nishioka, N. C. Derecki and M. P. Maher, *Sci. Rep.*, 2019, **9**, 12692.

17 J. Suzuki, K. Kanemaru and M. Iino, *Biophys. J.*, 2016, **111**, 1119–1131.

18 E. Neher and B. Sakmann, *Nature*, 1976, **260**, 799–802.

19 J. Gao, C. Liao, S. Liu, T. Xia and G. Jiang, *J. Nanobiotechnol.*, 2021, **19**, 1–18.

20 C. L. Hill and G. J. Stephens, *Patch Clamp Electrophysiology: Methods and Protocols*, 2021, pp. 1–19.

21 J. Patti and C. Montemagno, *Nanotechnology*, 2007, **18**, 325103.

22 V. R. Patel, A. M. Salinas, D. Qi, S. Gupta, D. J. Sidote and M. P. Goldschen-Ohm, *Nat. Commun.*, 2021, **12**, 6459.

23 K. Takemura, *Biosensors*, 2021, **11**, 250.

24 C. Zhu, X. Luo, W. V. Espulgar, S. Koyama, A. Kumanogoh, M. Saito, H. Takamatsu and E. Tamiya, *Micromachines*, 2020, **11**, 107.

25 W. H. Kim, J. U. Lee, S. Song, S. Kim, Y. J. Choi and S. J. Sim, *Analyst*, 2019, **144**, 1768–1776.

26 Z. Wang, Y. Xianyu, W. Liu, Y. Li, Z. Cai, X. Fu, G. Jin, Y. Niu, C. Qi and Y. Chen, *Anal. Chem.*, 2019, **91**, 6769–6774.

27 N. Khansili, G. Rattu and P. M. Krishna, *Sens. Actuators, B*, 2018, **265**, 35–49.

28 A. Brecht and G. Gauglitz, *Biosens. Bioelectron.*, 1995, **10**, 923–936.

29 H. H. Nguyen, J. Park, S. Kang and M. Kim, *Sensors*, 2015, **15**, 10481–10510.

30 A. Samanta, T. E. Hughes and V. Y. Moiseenkova-Bell, *Membrane protein complexes: Structure and function*, 2018, pp. 141–165.

31 K. Talavera, J. B. Startek, J. Alvarez-Collazo, B. Boonen, Y. A. Alpizar, A. Sanchez, R. Naert and B. Nilius, *Physiol. Rev.*, 2020, **100**, 725–803.

32 A.-P. Koivisto, M. G. Belvisi, R. Gaudet and A. Szallasi, *Nat. Rev. Drug Discovery*, 2022, **21**, 41–59.

33 K. Gerhold and D. Bautista, *J. Physiol.*, 2008, **586**, 3303.

34 P. B. Johnson and R.-W. Christy, *Phys. Rev. B: Solid State*, 1972, **6**, 4370.

35 X. Zhang, J. Qiu, X. Li, J. Zhao and L. Liu, *Appl. Opt.*, 2020, **59**, 2337–2344.

36 R. Naert, A. López-Requena and K. Talavera, *Int. J. Mol. Sci.*, 2021, **22**, 11460.

37 T. R. H. Büch, E. A. M. Schäfer, M.-T. Demmel, I. Boekhoff, H. Thiermann, T. Gudermann, D. Steinritz and A. Schmidt, *Chem.-Biol. Interact.*, 2013, **206**, 462–471.

38 L. J. Macpherson, A. E. Dubin, M. J. Evans, F. Marr, P. G. Schultz, B. F. Cravatt and A. Patapoutian, *Nature*, 2007, **445**, 541–545.

39 S. Luostarinen, M. Hämäläinen, N. Hatano, K. Muraki and E. Moilanen, *Pulm. Pharmacol. Ther.*, 2021, **70**, 102059.

40 E. Fernandes, M. Fernandes and J. Keeble, *Br. J. Pharmacol.*, 2012, **166**, 510–521.

41 J. Marmolejo, A. Canales, D. Hanstorp and R. Méndez-Fragoso, *Phys. Rev. Lett.*, 2023, **130**, 043804.

42 D. Baumgardner, S. Abel, D. Axisa, R. Cotton, J. Crosier, P. Field, C. Gurganus, A. Heymsfield, A. Korolev and M. Kraemer, *Meteorol. Monogr.*, 2017, **58**, 9.1–9.23.

43 J. C. Fraire, S. Stremersch, D. Bouckaert, T. Monteyne, T. De Beer, P. Wuytens, R. De Rycke, A. G. Skirtach, K. Raemdonck and S. De Smedt, *ACS Appl. Mater. Interfaces*, 2019, **11**, 39424–39435.

44 J. Alvarez-Malmagro, G. García-Molina and A. López De Lacey, *Sensors*, 2020, **20**, 3393.

45 B. Munteanu, F. Harb, J.-P. Rieu, Y. Berthier, B. Tinland and A.-M. Trunfio-Sfarghiu, *Eur. Phys. J. E: Soft Matter Biol. Phys.*, 2014, **37**, 1–8.

46 A. Velikonja, P. B. Santhosh, E. Gongadze, M. Kulkarni, K. Eleršič, Š. Perutkova, V. Kralj-Iglič, N. P. Ulrih and A. Iglič, *Int. J. Mol. Sci.*, 2013, **14**, 15312–15329.

47 E. Irajizad and A. Agrawal, *Biomech. Model. Mechanobiol.*, 2018, **17**, 103–109.

48 A. Agrawal and D. J. Steigmann, *Continuum Mech. Thermodyn.*, 2009, **21**, 57–82.